Clouds and the Earth's Radiant Energy System (CERES) FluxByCldTyp Edition 4 Data Product

Moguo Sun,[a] David R. Doelling,[b] Norman G. Loeb,[b] Ryan C. Scott,[b] Joshua Wilkins,[a]
Le Trang Nguyen,[a] and Pamela Mlynczak[a]

[a] Science System and Applications Inc., Hampton, Virginia
[b] NASA Langley Research Center, Hampton, Virginia

ABSTRACT: The Clouds and the Earth's Radiant Energy System (CERES) project has provided the climate community 20 years of globally observed top of the atmosphere (TOA) fluxes critical for climate and cloud feedback studies. The CERES Flux By Cloud Type (FBCT) product contains radiative fluxes by cloud type, which can provide more stringent constraints when validating models and also reveal more insight into the interactions between clouds and climate. The FBCT product provides 1° regional daily and monthly shortwave (SW) and longwave (LW) cloud-type fluxes and cloud properties sorted by seven pressure layers and six optical depth bins. Historically, cloud-type fluxes have been computed using radiative transfer models based on observed cloud properties. Instead of relying on radiative transfer models, the FBCT product utilizes Moderate Resolution Imaging Spectroradiometer (MODIS) radiances partitioned by cloud type within a CERES footprint to estimate the cloud-type broadband fluxes. The MODIS multichannel derived broadband fluxes were compared with the CERES observed footprint fluxes and were found to be within 1% and 2.5% for LW and SW, respectively, as well as being mostly free of cloud property dependencies. These biases are mitigated by constraining the cloud-type fluxes within each footprint with the CERES Single Scanner Footprint (SSF) observed flux. The FBCT all-sky and clear-sky monthly averaged fluxes were found to be consistent with the CERES SSF1deg product. Several examples of FBCT data are presented to highlight its utility for scientific applications.

KEYWORDS: Cloud forcing; Radiation budgets

1. Introduction

One of the greatest challenges in climate model projections of warming in response to anthropogenic forcing is the representation of clouds and their interactions with Earth's radiation budget in climate models (Boucher et al. 2013). Cloud processes occur over a range of time and space scales, which makes them difficult to model. Climate models agree that feedbacks collectively amplify the surface temperature response to external forcing, but the strengths of the feedbacks vary greatly among models owing to uncertainties in cloud feedbacks (Soden and Held 2006; Webb et al. 2013; Dufresne and Bony 2008; Zelinka et al. 2020). Given the large intermodel spread in cloud feedbacks, it is reasonable to turn to observations to help improve the representation of clouds in climate models.

Early attempts at using satellite observations to evaluate climate models involve calculating monthly regional averages of cloud radiative effect (CRE) from broadband radiometers (Ramanathan et al. 1989; Harrison et al. 1990). Passive satellite imagers have also been used to produce histograms of cloud-top pressure and cloud optical depth (Rossow and Schiffer 1991, 1999) that could be compared with climate models using "simulators" designed to emulate the satellite retrievals (Klein and Jakob 1999; Webb et al. 2001). Both approaches have been shown to be useful in understanding model biases related to clouds (Zhang et al. 2005; Wyant et al. 2006) and the influence of different cloud types on Earth's radiation budget (Ockert-Bell and Hartmann 1992; Hartmann et al. 1992). A logical extension to the earlier approaches involves using a radiative transfer model initialized with satellite cloud retrievals to directly determine radiative fluxes for different cloud types (Chen et al. 2000). This approach enables a more direct determination of the radiative effects of individual cloud types on Earth's radiation budget by separating the effects of clouds from other atmospheric and surface contributions. Cloud properties and associated radiative fluxes that are stratified into different cloud types provide more stringent constraints when validating models and also reveal more insights into the impact of clouds on climate. An extension to the Chen et al. (2000) approach is described in Zhou et al. (2013), who used radiative transfer model-based cloud radiative kernels (Zelinka et al. 2012) to calculate the TOA flux anomaly from the cloud fraction anomaly for clouds with a particular cloud-top pressure and optical depth as determined from Moderate Resolution Imaging Spectroradiometer (MODIS) observations. Cloud radiative kernels describe the change in overcast cloud radiative effect per unit change of cloud fraction within prescribed cloud-top pressure and optical depth ranges. This approach is much more computationally efficient compared to making explicit radiative transfer model calculations, but uncertainties are larger.
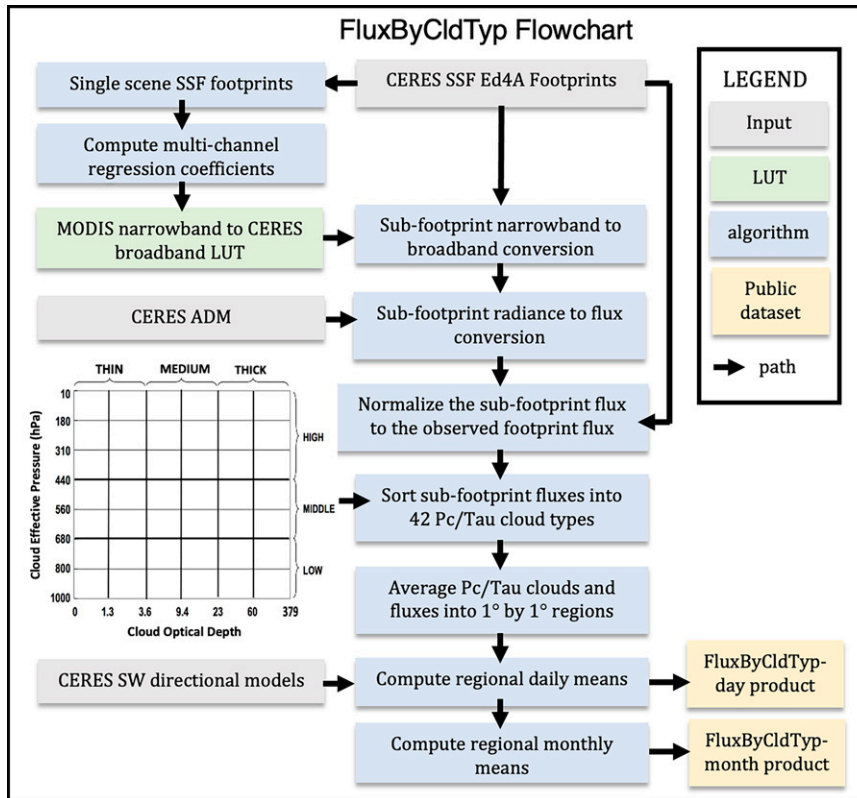

FIG. 1. The CERES FBCT flowchart. The FBCT cloud effective pressure by optical depth cloud types are also shown in the center-left portion and follows the ISCCP D1 product. LUT refers to the narrowband to broadband coefficient lookup table. FluxByCldTyp-day and FluxByCldTyp-month are the designated CERES Ed4 product names.

Cole et al. (2011) introduced a different method for determining TOA radiative fluxes by cloud type that avoids the use of radiative transfer models altogether. Instead, coincident CERES footprint fluxes and MODIS radiances from subfootprint cloud layers exposed to space are directly converted to cloud-layer radiative fluxes. The radiative fluxes are then sorted according to MODIS-derived cloud-top pressures and optical depths. Radiative fluxes from a given cloud exposed to space provide information about the integrated effect of underlying cloud whose details are generally unknown. Cole et al. (2011), and later Eitzen et al. (2017), developed climate model "flux-by-cloud-type simulators" to compare against the observed fluxes as a function of cloud type to demonstrate the utility of the approach.

In this study, we revisit Cole et al. (2011) and introduce several refinements to improve both the accuracy and utility of that approach. The updated algorithm is used to produce a new CERES data product, called the CERES FluxByCldTyp (FBCT) product, that is processed for the entire CERES record and is publicly available alongside other standard CERES data products. We present the FBCT methodology in section 2 and highlight the refinements made to what is described in Cole et al. (2011). Results and evaluation of the FBCT algorithm are provided in section 3. We also provide a discussion of various scientific applications of the FBCT product in section 4 and provide conclusions in section 5.

2. Data and methods

The CERES FBCT product follows closely the Cole et al. (2011) methodology. Figure 1 presents the FBCT product flowchart and provides an overview of the inputs and algorithms needed for FBCT processing. Section 2a describes the CERES SSF instantaneous footprint product, which is the basis for FBCT processing. Section 2b discusses the MODIS narrowband radiance to flux conversion. Section 2c describes how the footprint fluxes are then sorted into cloud effective pressure (radiative cloud top) and optical depth cloud types and spatially averaged into 1° regions. Section 2d details how the regional instantaneous cloud-type fluxes are averaged into daily and monthly means.

a. CERES SSF data product

The CERES Single Scanner Footprint (SSF) Edition 4A dataset is the main input to the FBCT product. The SSF product contains the observed CERES instrument 20-km nominal footprint TOA radiances, fluxes, and MODIS cloud properties. The CERES instruments observe the Earth shortwave

reflected radiance and longwave emitted radiance. The CERES onboard calibration systems ensure that the CERES instrument calibration is stable while in orbit (Loeb et al. 2016). The CERES observed radiances are converted to fluxes using empirical angular directional models (ADMs) (Su et al. 2015a,b) based on the MODIS imager cloud retrievals (Minnis et al. 2008, 2011a,b). The CERES MODIS cloud retrievals were designed to facilitate ADM flux accuracy and are not the official Goddard MODIS Science Team cloud properties. The CERES cloud retrieval algorithm is designed to minimize the number of nonretrieved pixels identified by the cloud mask in order to avoid any possible systematic biases that can occur when cloudy pixels from complex scenes are omitted, e.g., pixels near cloud edges (see CERES 2021, their Fig. 3-3). The FBCT utilizes both the *Terra* and *Aqua* SSF datasets. The *Terra* and *Aqua* satellites are in sun-synchronous orbits having a local equator crossing time of 1030 and 1330 LT, respectively. By combining both morning *Terra* and afternoon *Aqua* observations, the FBCT product provides robust daily flux estimates over diurnally varying maritime stratus and land afternoon convection regions.

The CERES clouds available on the SSF product are based on daytime and nighttime cloud retrieval algorithms. The daytime retrieval algorithm utilizes MODIS visible and IR channels, whereas the nighttime retrieval relies on IR channels only. IR-only channel cloud retrievals are limited to optical depths less than 4 (Minnis et al. 2011a), which limits the sampling of the optically thick clouds at night. Due to the nature of daytime and nighttime cloud retrieval differences, the CERES FBCT product utilizes only daytime footprints with solar zenith angles (SZA) less than 82° to avoid twilight conditions, ensuring consistent cloud-type classification.

The SSF product also contains the Global Modeling and Assimilation Office (GMAO)'s Goddard Earth Observing System Data Assimilation System (GEOS-DAS; V5.4.1) product (Rienecker et al. 2008) that provides the associated meteorological parameters for each CERES footprint. The effective pressure of the cloud retrieval to determine the FBCT cloud type and the total precipitable water (PW) utilized in the narrowband to broadband relationships are based on the GMAO profile. The surface type classification used in the FBCT narrowband to broadband relationships are determined from the 17 International Geosphere Biosphere Programme (IGBP) static surface/biome types are used to assign each footprint its surface type. Polar barren/desert type was classified as tundra (type 18). In addition to the IGBP permanent snow type (15), the sea ice (type 19) and daily land snow (type 20) coverages are added based on microwave maps from the National Snow and Ice Data Center (NSIDC) (Brodzik and Stewart 2016). The incoming solar daily irradiance is from the Solar Radiation and Climate Experiment, Total Solar Irradiance (SORCE TSI) (Kopp et al. 2005).

b. MODIS narrowband radiance to flux conversion

The CERES footprint is divided into subregions based upon the individual MODIS pixel-level cloud retrievals as shown in Fig. 2. The footprint is first divided into clear and cloudy sections. The cloud section is further divided into two
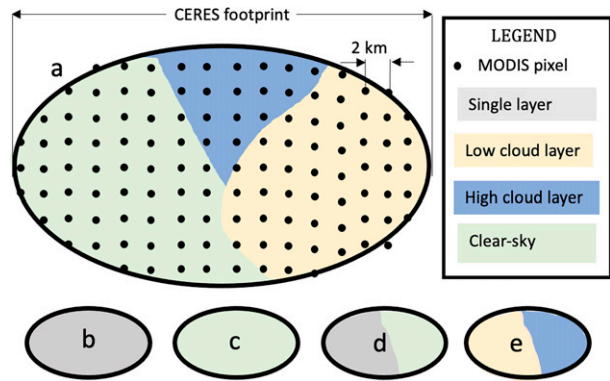

FIG. 2. Schematic of the CERES footprint (20-km nominal resolution). The MODIS pixel-level (subsetted 2-km nominal resolution) cloud retrievals determine the subfootprint- or cloud-layer and clear-sky boundaries as denoted in the legend. The cloud layers must have a separation of more than 50 hPa to be considered. (a),(d),(e) Classified as multiscene footprints. (b),(c) Classified as single-scene footprints. The narrowband to broadband coefficients are determined from the single-scene footprints and are applied to the corresponding subfootprint-scene type of multiscene footprints. Note that a CERES footprint contains about 160, 305, and 345 MODIS pixels at nadir, on average, and at maximum, respectively.

nonoverlapping cloud layers if the cloud effective pressure is greater than 50 hPa between layers. Therefore, each CERES footprint has the possibility of being divided into three subfootprint-scene types (see Fig. 2a). The mean MODIS pixel-level cloud properties and channel radiances are averaged for each subfootprint region.

Following Cole et al. (2011), the CERES footprint flux (Flux$_{\text{footprint}}$) is computed from the subfootprint-scene types as follows:

$$\text{Flux}_{\text{footprint}} = (1 - f_{\text{lay1}} - f_{\text{lay2}})\text{Flux}_{\text{clear}} + f_{\text{lay1}}\text{Flux}_{\text{lay1}} + f_{\text{lay2}}\text{Flux}_{\text{lay2}}, \tag{1}$$

where f_{lay1} and f_{lay2} are the cloud fraction for cloud-layer 1 and 2, respectively. Flux$_{\text{clear}}$, Flux$_{\text{lay1}}$, and Flux$_{\text{lay2}}$ are the clear-sky, layer 1, and layer 2 broadband fluxes derived from MODIS spectral channel radiances contained in the cloud-layer or clear-sky region of the CERES footprint. To convert the subfootprint MODIS channel radiance into broadband flux, Cole et al. (2011) assumed that the visible (0.65 μm) or IR (11 μm) MODIS radiance for the footprint is equal to the sum of the subfootprint MODIS radiance weighted by the clear-sky and cloud-layer fractions. This is similar to Eq. (1) but with the flux terms replaced by MODIS radiances. Their second assumption is that the ratio of the cloud-layer fluxes should equal the ratio of the corresponding mean MODIS channel radiances.

The CERES FBCT product avoids these assumptions by instead utilizing multiple MODIS spectral channel mean radiances to estimate the broadband radiance and then apply the CERES ADM to convert the broadband radiance to a flux. The MODIS narrowband channel radiances are used to

compute the subfootprint broadband radiances contained in multiscene footprints (Figs. 2a,d,e) based on empirical narrowband to broadband regressions derived from single-scene footprints (Figs. 2b,c), which have an associated CERES observed radiance and is described in the following section. This approach is similar to the CERES FBCT prototype product methodology employed by Eitzen et al. (2017) and is based on the Loeb et al. (2009) strategy to estimate the clear-sky fluxes from the clear-sky portion of partly cloudy footprints in order to enhance the clear-sky sampling for regions in persistent cloudy conditions. The use of empirical narrowband to broadband relationships to compute broadband radiances were also performed by Loeb and Manalo Smith (2005), Loeb et al. (2006), and Sun et al. (2006).

The SSF dataset parameter output only contains a subset of the total number of available MODIS channels, which limits the number of MODIS bands that can be used for the narrowband to broadband regressions. The SSF dataset provides the MODIS 0.47-, 0.65-, 0.86-, 11-, and 12-μm daytime channel radiances for each cloud layer within a CERES footprint and an additional seven MODIS channels for the clear-sky portion of a CERES footprint. To simplify the narrowband to broadband regression coding, the same five MODIS channels are used for the clear-sky and cloudy regions. The FBCT narrowband to broadband algorithm uses all five visible and IR channels to derive both SW and LW broadband radiances. As discussed in section 3a, using all 5 channels decreases the overall regression uncertainty from what can be achieved by using either visible or IR channel subsets. The use of both visible and IR channels may implicitly provide cloud information to derive the broadband radiances. We calculate the multivariate linear regression coefficients ($a_{channel}$) based on the 0.47-, 0.65-, 0.86-, 11-, and 12-μm MODIS channel radiances ($Rad_{channel}$) and the CERES footprint broadband radiance ($Rad_{footprint}$) as follows:

$$Rad_{footprint} = a_0 + \sum_{channel=1}^{5} a_{channel} Rad_{channel}. \qquad (2)$$

The *Terra* and *Aqua* MODIS coefficients were computed separately in order to take into account any calibration differences between sensors. A set of SW coefficients and LW coefficients are placed into lookup tables (LUTs).

The FBCT LUT narrowband to broadband coefficients are based on a 5-yr monthly climatology (2007–11) of overcast single-layer footprints having a cloud fraction greater than 99.9% (Fig. 2b) and clear-sky footprints having a cloud fraction less than 0.1% (Fig. 2c). The narrowband to broadband coefficients are stratified by month and into clear or overcast bins. Seven surface types are utilized: ocean, forests, savannas, grassland/crop, dark desert and bright desert, and snow/sea ice based on the aggregation of the IGBP types (see Table 2; Loeb et al. 2005). The SW coefficients are stratified into nine SZA bins in 10° increments from 0° to 82° (last bin 80° to 82°), seven view zenith angle (VZA) bins in 10° increments from 0° to 70°, and nine relative azimuth angle (RAA) bins in 20° increments from 0° to 180°. The LW coefficients utilize the

seven VZA bins and include four PW bins in increments from 0 to 1, 1 to 3, 3 to 5, and 5 to 10 cm (following Loeb et al. 2018a, their Table 4).

For single-scene-type footprints, the CERES observed footprint radiance is used directly. For the remaining multiscene footprints, the subfootprint MODIS radiances are converted to broadband radiances using the LUT narrowband to broadband coefficients. To avoid SW narrowband to broadband LUT bin discretization errors, linear interpolation between the LUT SZA, VZA, and RAA bins is performed. Similarly, linear interpolation between VZA and PW bins is performed to obtain the predicted LW broadband radiance. In case a LUT bin has insufficient sampling, neighboring well-sampled angular bin coefficients are used to estimate the broadband radiance.

The subfootprint MODIS broadband radiance is then converted to a broadband flux using the CERES ADMs. The subfootprint-layer (overcast) cloud or clear-sky properties, atmospheric and surface conditions as well the observed angles are used to select the appropriate CERES Edition 4 ADM scene type (Su et al. 2015a). The footprints with incomplete cloud information, where the number of nonretrieved cloud pixels exceeds 35%, are omitted in the FBCT processing. The individual subfootprint derived fluxes ($Flux_i$) are normalized to the CERES footprint observed flux ($Flux_{CERES}$) in the same manner as Eitzen et al. (2017) as shown in Eq. (3):

$$Flux_i^{normalized} = \left[\frac{Flux_{CERES}}{Flux_{footprint}} \right] \times Flux_i. \qquad (3)$$

Multiplying each of the subfootprint derived fluxes by the normalization ratio yields the normalized subfootprint fluxes $\left(Flux_i^{normalized} \right)$. The normalization ratio [bracketed terms in Eq. (3)] is the CERES footprint observed flux divided by the sum of the individual subfootprint fluxes weighted by their coverage (f_i) as computed on the right side of Eq. (1).

c. Cloud-type sorting and spatial averaging

Each of the single-scene overcast footprints and subfootprint cloud layers are assigned a cloud type according to the ISCCP DX cloud-type definitions based on cloud effective pressure and optical depth as shown in Fig. 1 (Rossow and Schiffer 1991, their Table 4). The 6 cloud optical depth bins are bound by 0.0–1.27, 1.27–3.55, 3.55–9.38, 9.38–22.63, 22.63–60.36, 60.36–378.65, and the seven cloud effective pressure boundaries are 1100–800, 800–680, 680–560, 560–440, 440–310, 310–180, 180–10 hPa. For each *Terra* or *Aqua* overpass, the cloud-type subfootprint and footprint cloud properties and fluxes located within a CERES 1° nested region are spatially averaged by weighting by their areal extent.

d. Daily and monthly averaging

Each instantaneous CERES footprint and subfootprint SW flux is converted into an equivalent daily mean 24-h flux by applying diurnal albedo models that account for albedo changes as a function of solar zenith angle (Young et al. 1998). The diurnal albedo models employed are the same as

for the SSF1deg product, which assumes that the observed cloud and atmospheric conditions remain constant over the day. The 1° regional cloud-type daily mean flux (Flux$_{\text{day}}$) is computed by averaging all of the subfootprint normalized [Eq. (3)] and overcast footprint (Fig. 2b) observed daytime regional *Terra* and *Aqua* fluxes $\left(\text{Flux}_i^{\text{normalized}}\right)$ having the same cloud type, area weighted by their cloud-type fraction (f_i) as follows:

$$\text{Flux}_{\text{day}} = \frac{\sum_{i=1}^{N_{\text{obs}}} \text{Flux}_i^{\text{normalized}} f_i}{\sum_{i=1}^{N_{\text{obs}}} f_i}, \quad f_{\text{day}} = \frac{\sum_{i=1}^{N_{\text{obs}}} f_i}{N_{\text{obs}}}, \quad (4)$$

where Flux$_{\text{day}}$ and f_{day} are the FBCT daily cloud-type flux and fraction for each cloud type, respectively, and N_{obs} is the number of 1° regional instantaneous *Terra* and *Aqua* measurements for the day. The sum of all the individual cloud-type and clear-sky f_{day} should equal 1.

The monthly mean individual cloud-type LW flux (LW$_{\text{mon}}$) is the summation of the cloud-type daily LW fluxes (LW$_{\text{day}}$) weighted by their daily cloud-type fraction (f_{day}) as follows:

$$\text{LW}_{\text{mon}} = \frac{\sum_{\text{day}=1}^{N_{\text{days}}} \text{LW}_{\text{day}} f_{\text{day}}}{\sum_{\text{day}=1}^{N_{\text{days}}} f_{\text{day}}}, \quad f_{\text{mon}} = \frac{\sum_{\text{day}=1}^{N_{\text{days}}} f_{\text{day}}}{N_{\text{days}}}, \quad (5)$$

where N_{days} is the number of days of the month. The cloud-type fraction for the month (f_{mon}) is the sum of individual daily cloud-type fractions divided by the number of days in the month. The summation of all the individual daily cloud-type and clear-sky f_{mon} should equal 1. For each cloud type, the effective temperature, effective pressure, IR emissivity, optical depth, liquid and ice fraction, water path, and particle size are averaged into daily and monthly means in the same manner as the LW fluxes.

To ensure that the monthly mean cloud-type SW flux is not skewed with the day of observation for regions where the solar incoming flux is rapidly changing over the month, the monthly mean cloud-type SW flux (SW$_{\text{mon}}$) is computed from the monthly mean cloud-type albedo (alb$_{\text{mon}}$) and the monthly mean solar incoming flux (Sol$_{\text{mon}}$) as follows:

$$\text{SW}_{\text{mon}} = \text{alb}_{\text{mon}} \text{Sol}_{\text{mon}}, \quad \text{Sol}_{\text{mon}} = \frac{1}{N_{\text{days}}} \sum_{\text{day}=1}^{N_{\text{days}}} \text{Sol}_{\text{day}}, \quad (6)$$

where the monthly mean solar incoming flux (Sol$_{\text{mon}}$) is the sum of the daily solar incoming fluxes (Sol$_{\text{day}}$) during the month regardless of cloud-type sampling divided by the number of days in the month (N_{days}). The monthly mean cloud-type albedo (alb$_{\text{mon}}$) is the daily cloud-type SW flux (SW$_{\text{day}}$) weighted by the daily cloud-type fraction (f_{day}) as follows:

TABLE 1. The January 2010 overcast single-layer footprint MODIS to CERES multichannel linear regression LW radiance RMS error (%) as a function of surface type (columns) and MODIS channel combinations (rows) used in the multichannel regression. IR 1 ch, IR 2 ch, and VIS + IR 5 ch denote the 12-μm channel; the 11-and 12-μm channels; and the 0.47-, 0.65-, 0.86-, 11-, and 12-μm channels, respectively. Note the reduction of the LW RMS error with increasing number of MODIS channels including adding the three visible channels with the two IR channels.

	Ocean	Savannah	Bright desert	Snow
IR 1 ch	3.00	3.50	2.57	3.44
IR 2 ch	2.75	3.08	2.22	3.40
IR+VIS 5 ch	2.52	2.86	1.90	2.65

$$\text{alb}_{\text{mon}} = \frac{\sum_{\text{day}=1}^{N\text{obs}_{\text{days}}} \text{SW}_{\text{day}} f_{\text{day}}}{\sum_{\text{day}=1}^{N\text{obs}_{\text{days}}} \text{Sol}_{\text{day}} f_{\text{day}}}, \quad (7)$$

where Nobs$_{\text{days}}$ is the number of days with albedo observations, whereas N_{days} used in Eq. (6) includes all days of the month, regardless of observations. Note that the albedo multiplied by the solar incoming flux equals the SW flux.

The clear-sky flux is computed in the same manner as if it were a cloud type. The all-sky fluxes and clouds are computed by weighting all 42 cloud types and clear-sky fluxes and clouds by their respective fractions. The FBCT-day product provides the number of cloud-type and clear-sky LW and SW observations to allow the user to determine if there is sufficient sampling for their application.

3. Results and validation

In the following we validate the SW and LW narrowband to broadband regression coefficients (section 3a) and TOA fluxes (section 3b) and check for FBCT product flux consistency across other CERES monthly averaged products (section 3c).

a. Narrowband to broadband radiance

Here we demonstrate the benefit of using both MODIS visible (0.47, 0.65, 0.86 μm) and IR channels (11 and 12 μm) in the SW narrowband to broadband multivariate regressions. In Table 1 we compare the LW RMS error using a single 12-μm IR channel (IR 1 ch), the two IR channels (IR 2 ch), and the five visible and IR channels (IR+VIS 5 ch) as a function of surface type across all view angles observed during January 2010. The single 12-μm channel had the lowest RMS error across all scene types among the five channels. The additional IR 11-μm window channel reduce the LW RMS by ~10% over the single 12-μm channel, except over snow. Including the three visible channels further reduce the LW RMS error over using the two IR channels by ~10%, except over snow where the reduction is ~20%. More than likely, the addition of the visible channels infers the cloud optical depth, which

TABLE 2. The January 2010 overcast single-layer footprint MODIS to CERES multichannel linear regression SW radiance RMS error (%) as a function of surface type (columns) and MODIS channel combinations (rows) used in the multichannel regression. VIS 1 ch, VIS 3 ch, and VIS + IR 5 ch denote the 0.65-μm channel; the 0.47-, 0.65-, and 0.86-μm channels; and the 0.47-, 0.65-, 0.86-, 11-, and 12-μm channels; respectively. Note the reduction of the SW RMS error with increasing number of MODIS channels including adding the two IR channels with the three visible channels.

	Ocean	Savannah	Bright desert	Snow
VIS 1 ch	3.40	3.01	2.34	2.60
VIS 3 ch	3.17	2.82	2.13	2.23
VIS + IR 5 ch	2.66	2.38	1.72	1.99

helps determine the IR emissivity and cloud effective pressure. Unfortunately, the MODIS water vapor channel (6.7 μm) radiances were not available for cloud layers on the SSF product and therefore not used in Eq. (2) to compute the cloud-type LW radiances. Any residual cloud-type LW flux bias from not including the water vapor channel radiances should be resolved by normalizing the predicted LW flux with the observed footprint LW flux, since the water vapor burden should not vary much over the 20-km nominal footprint.

Similarly in Table 2 we compare the SW narrowband to broadband regression RMS error using a single 0.65-μm visible channel (VIS 1 ch), the three visible channels (VIS 3 ch), and the five visible and IR channels (VIS + IR 5 ch) as a function of surface type across all view and solar angles observed during January 2010. For all surface types excluding snow, the 0.65-μm channel had the lowest single channel RMS error. Adding the 0.47- and 0.86-μm channels reduces the SW RMS error between 7% and 14% depending on surface types. The five-channel SW RMS error is diminished between 16% and 20%, except over snow. This is in part because the IR channels provide crude cloud height information that is helpful to estimate the SW NIR water vapor absorption. The smaller 10% SW RMS reduction over snow when including the IR channels is probably due to that the snow reflectance is more predictable over visible wavelengths, and the cold atmospheric conditions limit the water vapor variability.

b. Narrowband to broadband flux

Here we validate the FBCT narrowband to broadband algorithm by comparing the derived footprint flux summed from the individual subfootprint narrowband to broadband fluxes with the observed flux sampled from all multiscene footprints. This comparison is made prior to applying the normalization to the observed fluxes in Eq. (3), which will mitigate most of the flux differences discussed in this subsection. The differences provide an indication of how large a correction is necessary during the normalization step. The LW narrowband to broadband coefficients are binned by VZA, clear or overcast, surface type, and PW, not by cloud properties. To ensure there are no systematic cloud dependencies embedded in the LW derived fluxes, Fig. 3 shows the LW derived and observed footprint LW flux differences plotted as a function

of cloud fraction, cloud effective pressure, cloud effective temperature, cloud optical depth, PW, SZA, VZA, and surface type for January 2010. The derived and observed LW flux bias and standard deviation was within 1% (2.5 W m^{-2}) and 3% (8 W m^{-2}), respectively, for all eight parameters. The bias and standard deviation are uniform over the range of the eight parameters, except for PW values greater than 6 cm. The low PW values in Fig. 3e are found over Antarctica.

Similarly, the SW narrowband to broadband derived and observed fluxes are compared from all multiscene footprints in Fig. 4 and plotted as a function of cloud properties, PW, SZA, VZA, and surface type. The SW narrowband to broadband algorithm is binned according to SZA, VZA, RAA, clear/overcast, and surface type. The January 2010 SW flux bias was within 2.5% (6.25 W m^{-2}) for the parameters in Fig. 4 over the entire parameter range, except for cold cloud effective temperatures (<220 K in Fig. 4c) and for thin optical depth clouds (<0.4 or a log optical depth < −1 in Fig. 4d). The SW flux standard deviation was mostly within 8% or 20 W m^{-2}. Figure 4a reveals that the partly cloudy footprints are the source of the negative bias, which suggests that the partly cloudy or multiscene footprints, which account for two thirds of all footprints, may contain certain cloud conditions not found in single-scene footprints used to compute the cloudy SW narrowband to broadband coefficients.

We note that single-scene footprints are not distributed evenly across the globe. Figure 5 shows the January 2010 regional ratio of single-scene and total footprints and clearly shows the uneven spatial sampling. Large parts of the tropics contain less than 20% single-scene footprints. Figure 6a shows the geographical distribution of the derived minus the observed instantaneous SW flux bias for multiscene footprints. The negative SW flux bias band between 10° and 30°N over ocean seems to be associated with sparse sampling of single-scene footprints (Fig. 5). Similarly, the lack of single-scene footprints (Fig. 5) observed over the Tibetan Plateau more than likely explains the large negative bias in Fig. 6a. The SW derived fluxes over land snow (Russia and Canada) and sea ice (Hudson Bay and Antarctica) have large positive derived fluxes, where the SW LUT coefficients were more than likely determined over the permanent snow conditions of Antarctica and not suitable for land snow or sea ice conditions.

The overall LW bias is smaller than the SW derived bias and is close to zero (Fig. 6b). Unlike the SW bias, the LW bias is not associated with partly cloudy footprints (Fig. 3a). It is unknown why the Peruvian maritime regions have a negative LW bias given the large frequency of single-scene footprints. Again, most of these prenormalized flux biases shown in Figs. 3, 4, 5, and 6 will be mitigated after applying Eq. (3).

c. Consistency with other CERES products

When all 42 FBCT cloud-type fluxes are combined with the clear-sky flux, they should be consistent with all-sky fluxes in other CERES products. For this consistency check, an SSF1deg dataset (Doelling et al. 2013) was processed with both *Terra* and *Aqua* observed fluxes. We also highlight the algorithm differences between the two products. For example,
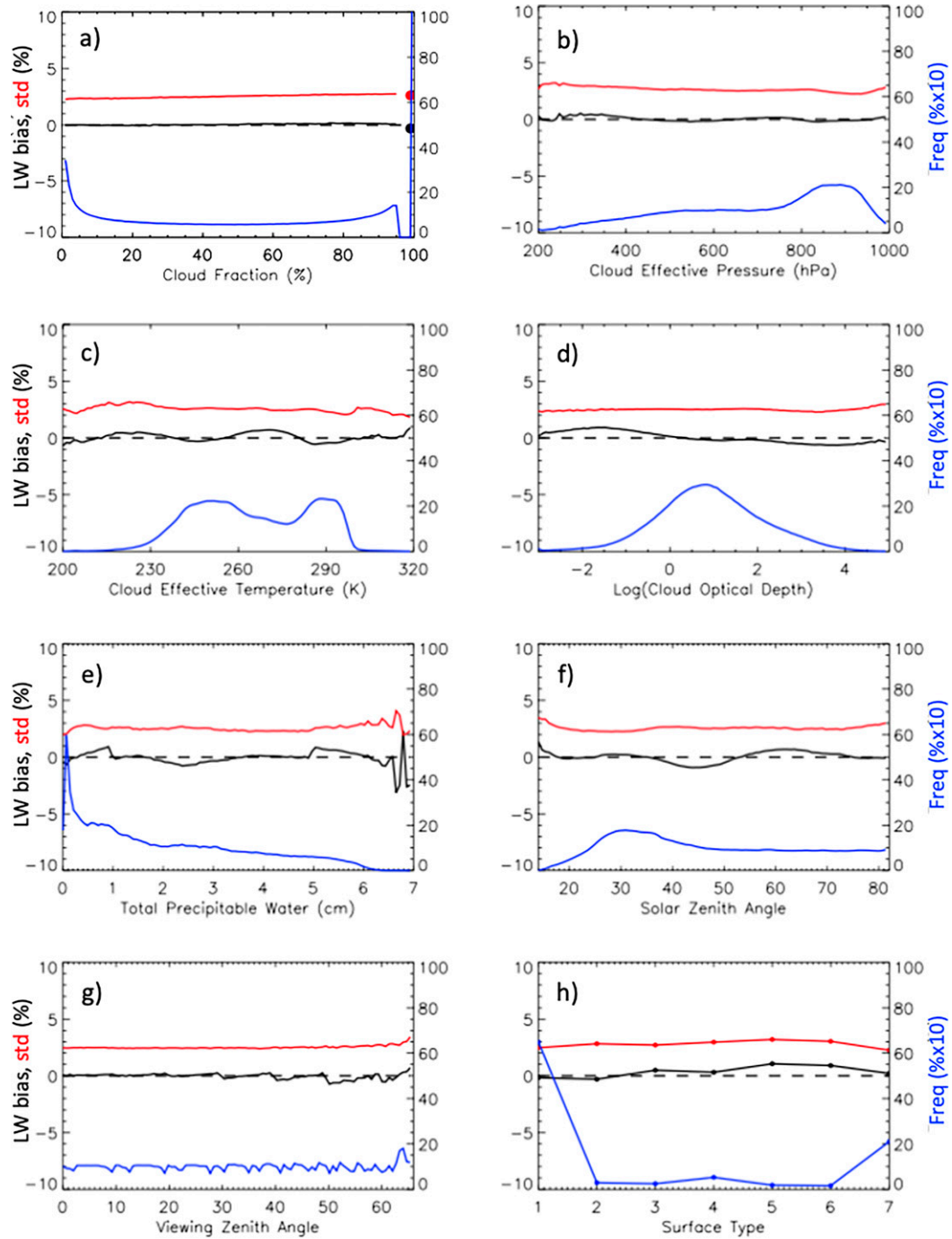
FIG. 3. The January 2010 (sampled by every third day) narrowband to broadband derived and observed LW (multiscene) footprint flux bias (% black line), standard deviation (%; red line), and the frequency (% × 10; blue line; right axis) as a function of (a) cloud fraction (%), (b) cloud effective pressure (hPa), (c) cloud effective temperature (K), (d) logarithm of the cloud optical depth, (e) total precipitable water (cm), (f) SZA (°), (g) view zenith angle (°), (h) surface type, where 1 = ocean, 2 = forest, 3 = savannah, 4 = grass, 5 = dark desert, 6 = bright desert, 7 = snow/ice specific to January 2010. Note that cloud-type fractions of 100% are considered single-scene footprints.
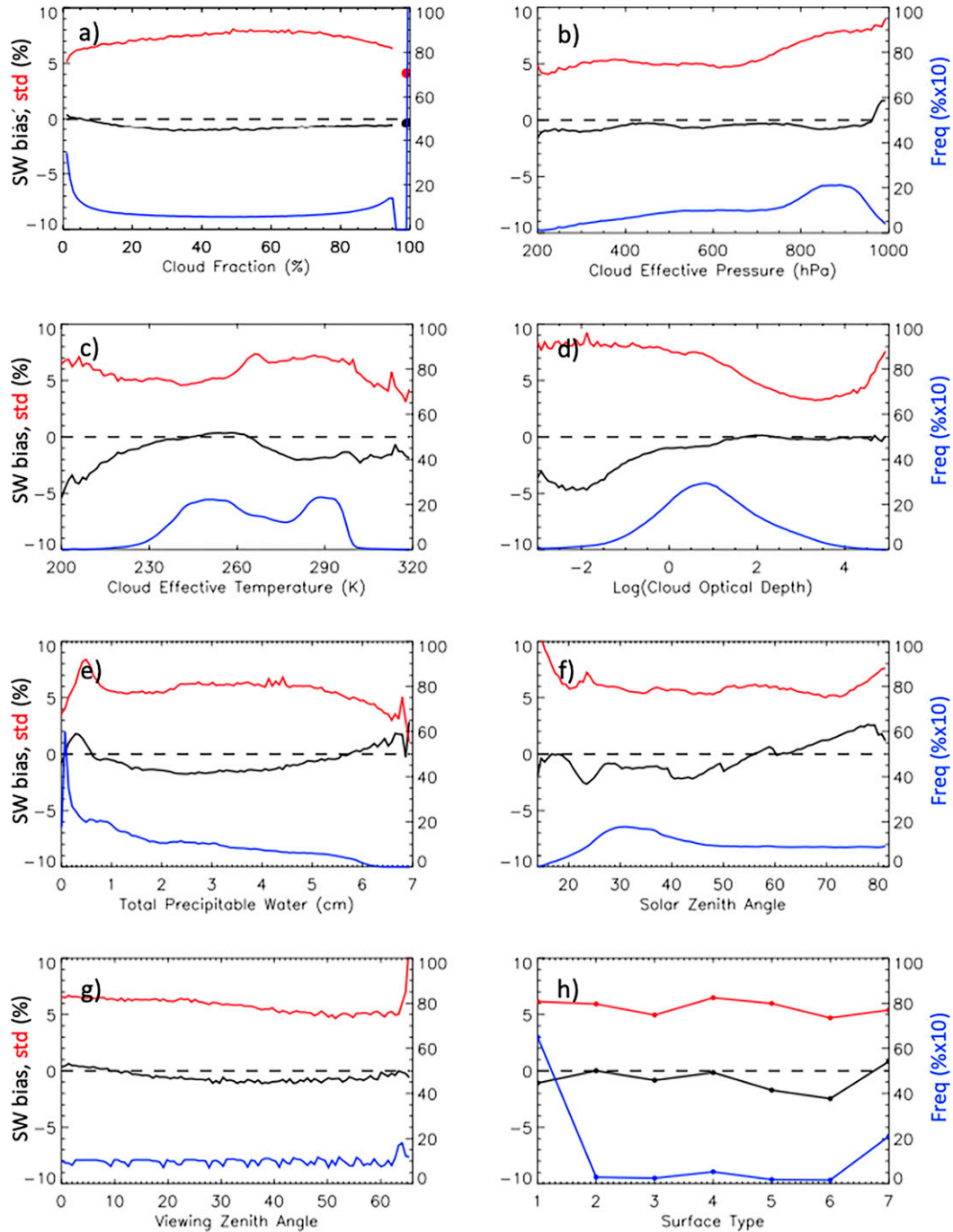
FIG. 4. As in Fig. 3, but for SW flux.

the FBCT product SW and LW fluxes only include footprints with SZAs less than 82° in order to avoid twilight and night-time cloud retrievals. The SSF1deg SW fluxes use all footprints with a SZA less than 86.5°. The SSF1deg LW fluxes utilize all observed daytime and nighttime footprints. During January 2010, there are two zonal domains where the FBCT SZA threshold greatly limits the number of observations compared with SSF1deg, located between 60° and 65°N and

between 68° and 75°S. The FBCT and SSF1deg total cloud amount, effective pressure and optical depth are very similar across all regions during January 2010, except for the zones impacted the SZA threshold (see CERES 2021, their Fig. 5.5).

Both the FBCT and SSF1deg monthly regional all-sky SW fluxes are based upon the same diurnal albedo models. The FBCT product simply averages all of the 24-h SW flux observations during the day, whereas the SSF1deg product
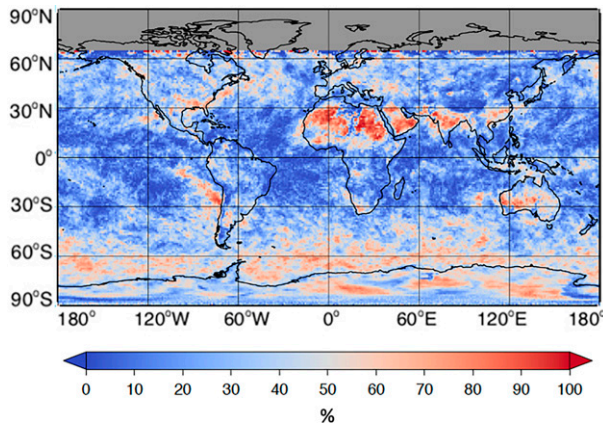
FIG. 5. The ratio of single-scene footprints divided by total footprints during January 2010 (sampled by every third day; %). Globally the ratio of single-scene footprints is one-third of the total footprints.

determines the daily mean by temporally interpolating using the diurnal albedo models between the sequential instantaneous albedos observed over the day. The SW flux noise about the date line in the difference between FBCT and SSF1deg in Fig. 7b is due to the calendar month GMT time boundary. At the date line, GMT midnight denotes local noon, whereas GMT noon denotes local midnight. The SSF1deg product utilizes nearby observed SW fluxes from the previous month and following month in order to temporally interpolate between sequential observations across the month time boundary. The FBCT product only uses measurements observed within the calendar month time boundary. The SW flux also differs between 68° and 75°S; this area is impacted by the FBCT SZA threshold of 82°.

Remarkably, whether the SW fluxes are temporally interpolated (SSF1deg) or the 24-h SW fluxes are simply averaged (FBCT), the SW regional monthly mean flux is very similar (Fig. 7b). The *Terra* and *Aqua* sun-synchronous orbits are well-placed and symmetric about noon, allowing simple averaging of the 24-h SW fluxes to compute the daily mean flux.

Also, both the FBCT and SSF1deg products compute the monthly mean albedo from the daily albedos using the same Eqs. (6) and (7).

The all-sky LW flux FBCT minus SSF1deg bias is displayed in Fig. 7d. The FBCT product overestimates the regional LW flux over land because it does not include the colder clear-sky nighttime observations. Over oceans the FBCT and SSF1deg regional bias is noisy because the SSF1deg product temporally interpolates between day and night sequential measurements, whereas the FBCT simply averages the daytime measurements. The exception is over maritime stratus regions (e.g., off the coast of Peru) where the cloud top and clear-sky ocean temperatures are similar and over Antarctica, where no nighttime measurements are observed during January.

The FBCT product increases the clear-sky sampling by incorporating subfootprint clear-sky fluxes (for cloud free areas of region) similar to the CERES EBAF product (Loeb et al. 2018a), whereas the SSF1deg product utilizes only completely clear footprints. The clear-sky subfootprint fluxes are located near cloud edges and are typically more humid and contain more aerosols than the larger 20-km nominal CERES clear-sky footprints. The increased atmospheric humidity near clouds tends to decrease the clear-sky LW flux, as shown in the large negative value (blue) swaths over tropical convection areas and midlatitude storm tracks in Fig. 7c. The increase in aerosols and 3D effects near clouds would likely increase the clear-sky SW flux, which are the positive values (red) shown in Fig. 7a over tropical convection and midlatitude storm tracks. These results are in agreement with Loeb et al. (2009, their Figs. 3e,f). A noteworthy difference between FBCT and EBAF is that to compute the CRE, FBCT uses the clear-sky flux derived from subfootprint clear-sky pixels while EBAF uses the clear-sky flux for the total region (Loeb et al. 2020b).

The FBCT, SSF1deg, and EBAF product all-sky and clear-sky monthly global mean SW and LW flux anomalies are compared from July 2002 to December 2018 in Fig. 8. Only regions with valid FBCT fluxes are averaged to determine the three products' global monthly means in Fig. 8, which shows excellent agreement of the products' global mean all-sky
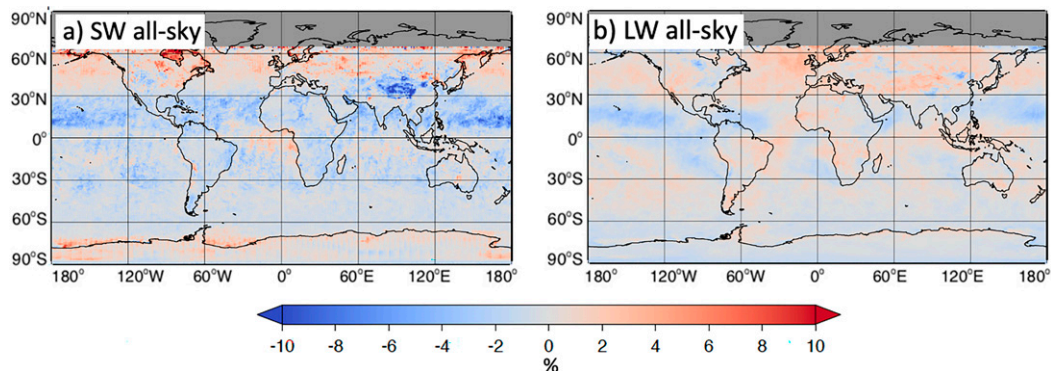

FIG. 6. The narrowband to broadband derived (multiple scene) minus observed (a) SW and (b) LW footprint instantaneous flux bias during (every third day of) January 2010 (%). Positive values indicate more SW reflection and LW emission to space.
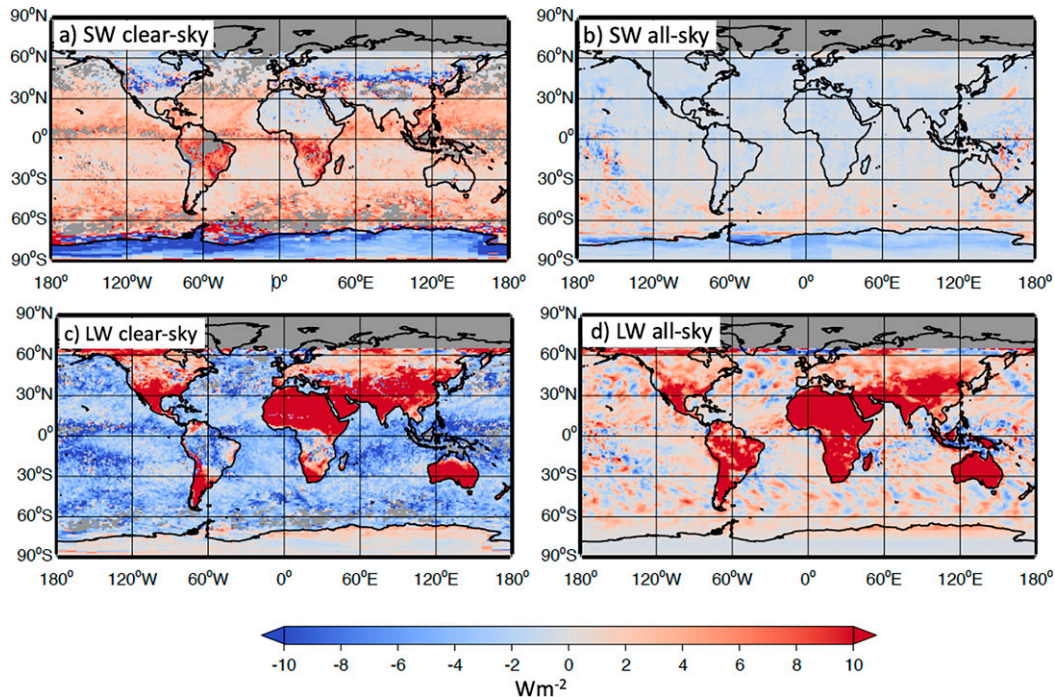
FIG. 7. The January 2010 FBCT-Month minus SSF1deg-Month (*Terra + Aqua*) for (a) all-sky SW, (b) clear-sky SW, (c) all-sky LW, and (d) clear-sky LW. Positive values indicate more SW reflection and LW emission to space.

and clear-sky SW flux anomalies. It is remarkable that the daytime-only FBCT all-sky and clear-sky LW flux anomalies are consistent with the EBAF and SSF1deg LW flux anomalies, which combine both day and night measurements. This is in agreement with Taylor and Loeb (2013), who state that most of the temporal LW flux variability is caused by the mean state conditions; little comes from the diurnal variability over time.

4. Applications and discussion

Potential applications of the FBCT product include monitoring cloud-type fluxes and coverage, validating climate model energetics by cloud type through the use of cloud simulators (Eitzen et al. 2017), and isolating cloud radiative effects and cloud–climate feedbacks by cloud type (Eitzen et al. 2008; Sun et al. 2012). In this section, we present several examples of the FBCT data to highlight its utility for scientific applications.

a. Radiative flux kernels

Zelinka et al. (2012) produced cloud-type radiative kernels to estimate cloud feedbacks to greenhouse warming simulated by global climate models. When multiplied by the change in cloud fraction associated with climate change, they provide an estimate of the anomalous cloud-induced radiative flux at TOA, and hence the cloud feedback. These cloud radiative kernels were computed as the overcast-sky cloud-type radiative effect (i.e., the clear-sky minus cloud-type (overcast) flux divided by 100%) using the Fu–Liou radiative transfer model

using idealized clouds and 20-yr zonal mean atmospheric profiles from Coupled Model Intercomparison Project phase 3 (CMIP3) control runs. Zhou et al. (2013) later produced a modified set of kernels to estimate the radiative impact of perturbations in satellite-observed cloud fields.

Here, we calculate a set of cloud radiative kernels using the observed FBCT clear-sky and cloud-type fluxes [see Scott et al. 2020, Eq. (6)]. Similar observation-based cloud radiative kernels have recently been presented by Yue et al. (2016) and Berry et al. (2019). The FBCT kernels are a function of calendar month, latitude, longitude, cloud effective pressure, and cloud optical depth. Figure 9 presents the annual and global mean FBCT cloud radiative kernels and compares them to those computed by Zhou et al. (2013). A positive value corresponds to a cloud radiative warming effect on climate, and vice versa. The LW kernels are positive for all cloud types, indicating that an increase in cloud fraction reduces the emission of thermal infrared radiation to space. Such reductions are especially pronounced for high and optically thick cloud types, as they emit as blackbodies at temperatures much colder than Earth's surface. The SW kernels are negative for all cloud types, indicating that an increase in cloud fraction enhances the reflection of solar radiation back to space. The net cloud radiative (LW+SW) kernels are negative for most cloud types owing to a dominance of the SW component, except for high thin cloud types.

While both sets of kernels show similar patterns and values, there are several differences worth noting. First, the CERES MODIS cloud algorithm only retrieves cloud properties for clouds with an optical depth above 0.25 (Minnis et al. 2011a);
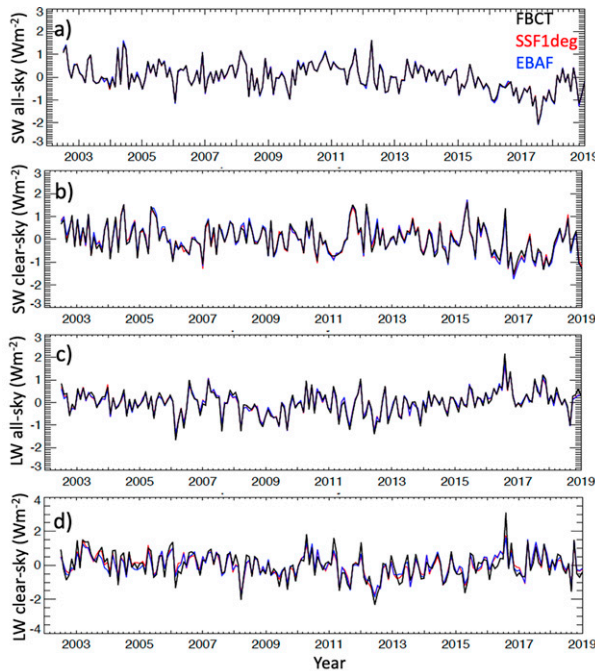
FIG. 8. The FBCT Ed4A (black line) and SSF1deg (*Terra* + *Aqua*) Ed4A (red line), and EBAF Ed4.1 (blue line) (a) all-sky SW, (b) clear-sky SW, (c) all-sky LW, and (d) clear-sky LW near-global mean deseasonalized flux anomalies from July 2002, computed from regions having observations with SZA < 82°. These are not true global means. Positive values indicate an increase in the SW reflection and LW emitted flux to space.

FBCT therefore does not include an optical depth bin for 0–0.3. The FBCT kernels are based on CERES MODIS observed clouds, whereas the Zhou et al. (2013) kernels are based on synthetic clouds and do not capture zonal flux variations. The FBCT LW kernel is based on daytime fluxes only, whereas the Zhou et al. (2013) LW kernel is based on a full 24-h diurnal average. FBCT also stratifies clouds vertically using cloud effective pressure instead of cloud-top pressure. Finally, although the FBCT fluxes are constrained by CERES observations, these fluxes are partitioned among different cloud types in the presence of observed surface and meteorological variations. Such conditions are usually held fixed when developing radiative kernels to isolate cloud from non–cloud radiative perturbations (Zelinka et al. 2012).

b. Partitioning the TOA CRE by cloud type

Since the early days of monitoring Earth's radiation budget via satellites, estimates of the CRE, defined as the clear-sky minus all-sky TOA radiative flux, have been used to study the role of clouds in Earth's climate (Ramanathan et al. 1989). Figure 10 shows the observed CRE climatology from FBCT computed as the clear-sky minus overcast-sky cloud-type flux difference times the cloud fraction in each bin. The results, summed over all 42 bins, are shown for the SW CRE (Fig. 10a), LW CRE (Fig. 10b), and net CRE (SW + LW; Fig. 10c). Subsequent panels show the relative contributions

of high-level clouds ($10 < p_c < 440$ hPa), midlevel clouds ($440 < p_c < 680$ hPa), and low-level clouds ($p_c > 680$ hPa). Low clouds dominate over the oceans and provide a strong radiative cooling effect on climate (Figs. 10c,l). They account for over 90% of the CRE in the maritime subsiding branches of the Hadley and Walker circulations and over 50% over the midlatitude oceans in each hemisphere. In contrast, over the world's major deserts trapping of outgoing LW radiation and only weak reflection of SW radiation by high-level clouds (Figs. 10d,e) yields a positive CRE, representing a weak warming effect on climate (Fig. 10c). In addition to climatological information, FBCT provides an ability to investigate cloud-type radiative variability associated with different climatic events.

c. Tropical cloud-radiative structures during El Niño–Southern Oscillation

The FBCT product can also be used for example to study CRE variations during El Niño events. Previous El Niño studies have often relied on climate model simulated fluxes rather than observations to estimate cloud-type radiative effects (Cess et al. 2001; Sun et al. 2012; Zhang et al. 2020). To demonstrate the utility of FBCT to quantify CREs during El Niño events, cloud-type fluxes were averaged over the tropical western Pacific (TWP) area bound by 5°S–10°N, 120°–170°E for all months with a Multivariate ENSO Index version 2 (MEI.v2; https://psl.noaa.gov/enso/mei/) greater than +0.5 and the July 2002 to December 2019 record mean was subtracted. Figure 11 shows histograms of cloud fraction, SW CRE, LW CRE and net CRE anomalies during El Niño conditions. As the center of deep convection shifts eastward to the central-eastern Pacific, reductions in high-level cloud cover in the TWP region induce positive SW CRE (Fig. 11b) and negative LW CRE (Fig. 11c) anomalies. The high-level net CRE anomaly shows nearly compensating SW and LW effects (Fig. 11d).

d. Twenty-first century low-cloud and radiation variability in the NE Pacific

Motivated by recent studies of low-cloud and climate variability in the NE Pacific (Loeb et al. 2018b, 2020a; Myers et al. 2018), as a final example of the possible scientific applications of FBCT data, Fig. 12 presents low-level CRE anomalies in the NE Pacific during the CERES record. Loeb et al. (2018b, 2020a) attribute an increase in TOA net downward radiation following the so-called global warming "hiatus" to reductions in low-level cloudiness in the Californian stratocumulus region. This change coincided with a shift in the sign of the Pacific decadal oscillation (PDO) from a negative to positive phase and encompassed the 2013–15 "marine heatwave" (Loeb et al. 2020a). During the negative PDO phase, prior to 2013/14, cool SSTs in the NE Pacific favored positive anomalies of low-level cloud cover that in turn helped maintain cool SSTs. With the emergence of the "marine heatwave," increases in SST promoted reductions in low-level cloud cover and positive low-level CRE anomalies, leading to a positive SST low-cloud feedback and an increase in SW absorption by
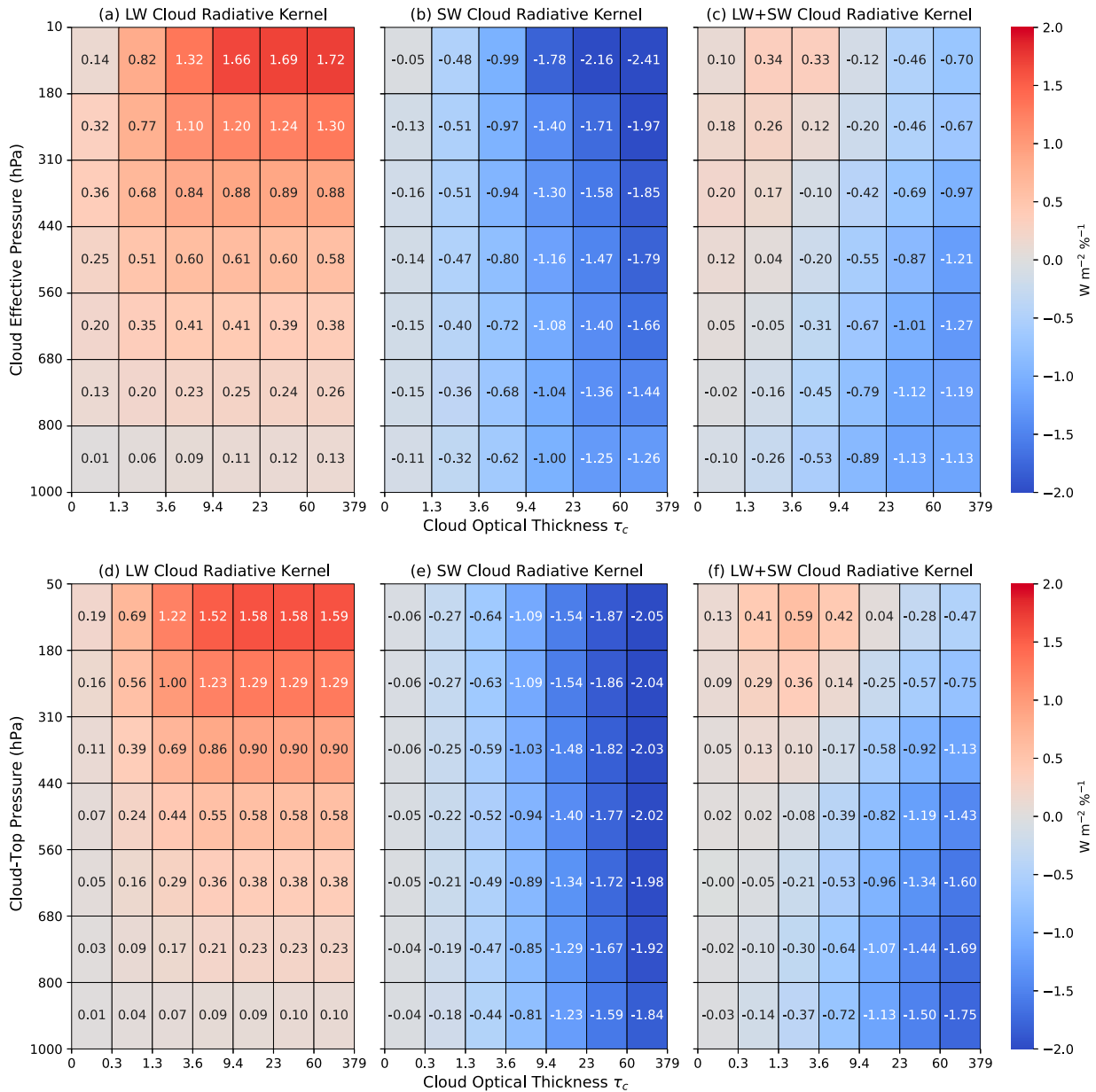
FIG. 9. CERES FluxByCldTyp annual and global area-weighted mean (a) LW, (b) SW, and (c) net cloud radiative kernels computed with respect to the July 2002 to July 2020 climatology expressed in units of W m^{-2} per percentage change in cloud fraction. (d)–(f) The corresponding Zhou et al. (2013) cloud radiative kernels. The SW kernel in (e) was mapped using the climatological clear-sky surface albedo (Zelinka et al. 2012) from CERES EBAF Ed4.1.

the climate system (Myers et al. 2018). As shown in the bottom panel of Fig. 12, the increase in SW absorption was largely attributed to decreases in low-level clouds having optical depths between 3.6–9.4 and 9.4–23.

5. Conclusions

The CERES project has thus far provided the climate community with over 20 years of globally observed TOA fluxes

and cloud properties. The CERES FBCT product now provides radiative fluxes by cloud type partitioned as a function of cloud optical depth and cloud effective pressure. This provides more stringent constraints to validate climate models and also enables new insight into the interactions between radiation, clouds, and climate. The FBCT fluxes utilize MODIS radiances categorized by cloud type within a CERES footprint to empirically determine the broadband cloud-type fluxes, and do not rely on the use of radiative transfer models.
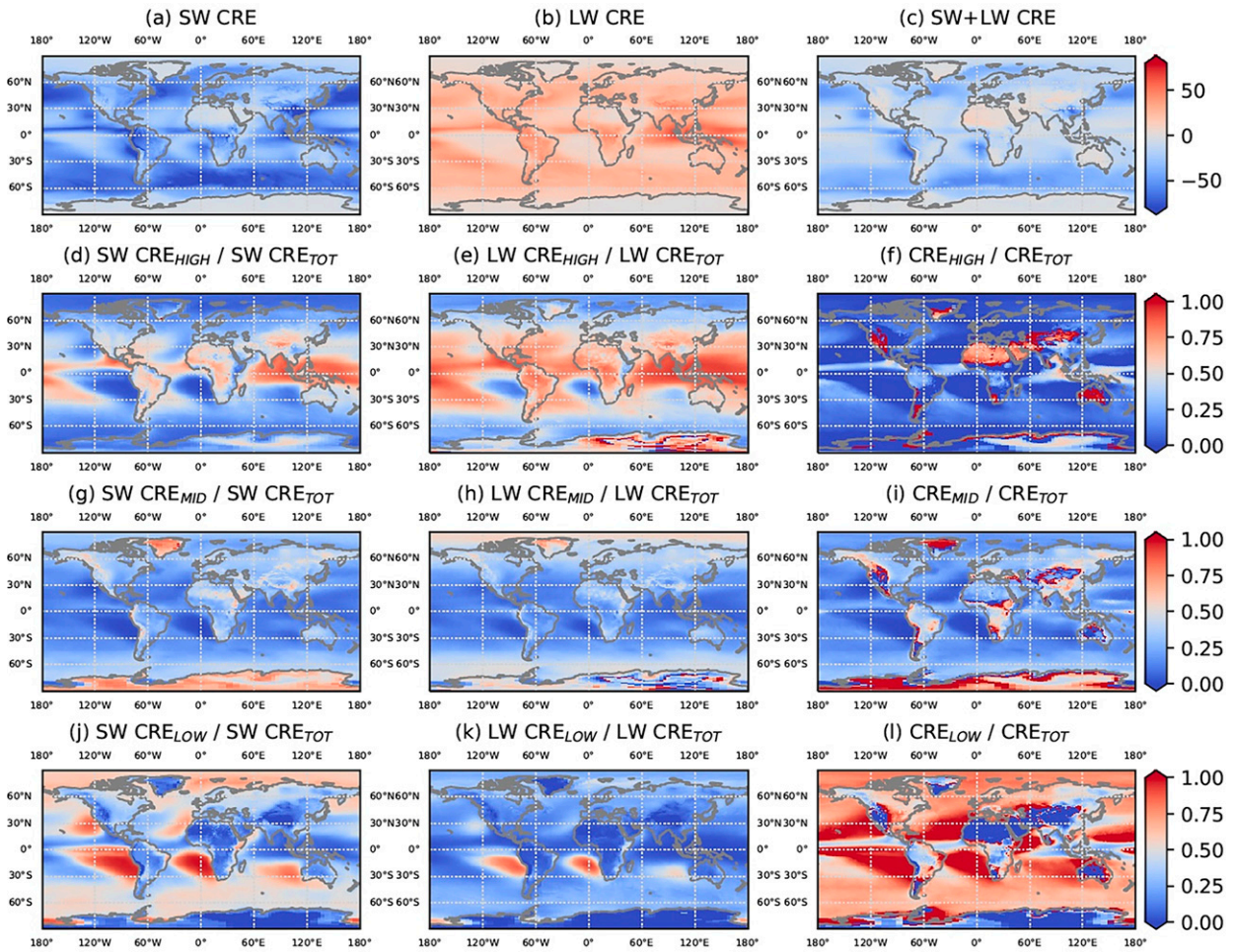
FIG. 10. Annual mean climatology of the (a) SW CRE, (b) LW CRE, and (c) net CRE at the top of the atmosphere from July 2002 to July 2020, along with the relative contributions from (d)–(f) high-level clouds, (g)–(i) midlevel clouds, and (j)–(l) low-level clouds.

To demonstrate the benefit of this approach, Cole et al. (2011), and later Eitzen et al. (2017), incorporated "flux-by-cloud-type simulators" in climate models and compared the resulting cloud-type fluxes with those based on MODIS and CERES. Here, we have improved upon the Cole et al. (2011) approach by utilizing multiple MODIS spectral channels

similar to the strategy of Loeb et al. (2009). Cole et al. (2011) only used a single MODIS channel to infer the cloud-type fluxes within a CERES footprint. The FBCT uses single-scene footprints to determine the MODIS narrowband to broadband radiance coefficients and applies the coefficients to the multiscene subfootprint MODIS channel radiances. The MODIS
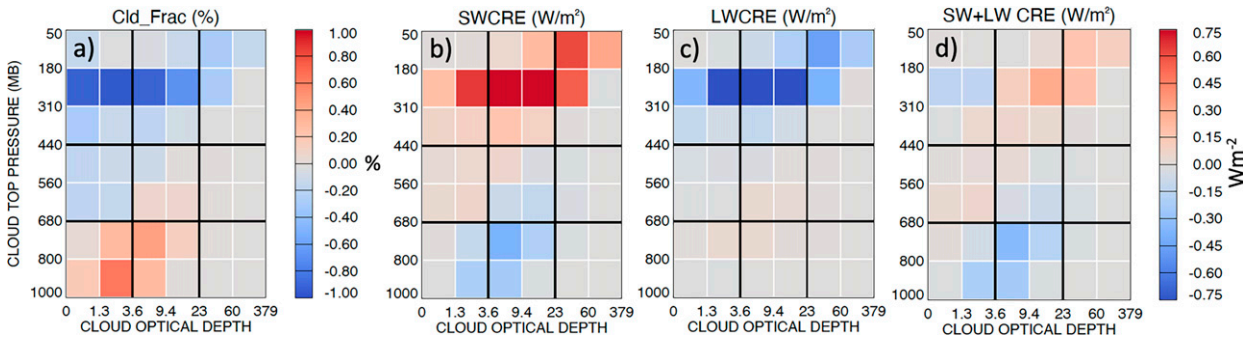

FIG. 11. The (a) cloud fraction and (b) SW CRE, (c) LW CRE, and (d) net CRE anomalies relative to the July 2002 to December 2019 FBCT record for composite El Niño events having MEI.v2 greater than 0.5 over the 5°S–10°N, 120°–170°E TWP domain.
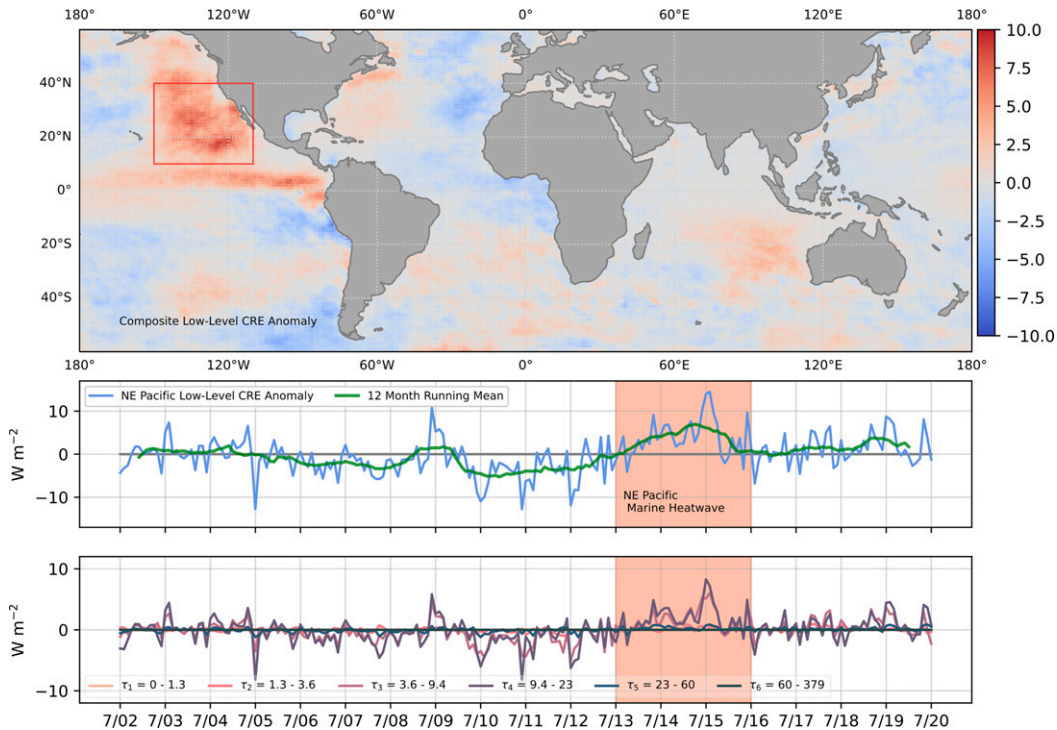
FIG. 12. (top) Composite low-level CRE anomalies during the 2013–15 NE Pacific marine heatwave. The red box highlights the NE Pacific analysis domain shown in subsequent panels, which present area-weighted average anomaly time series of the (middle) total low-level CRE and (bottom) the contributions from low-level clouds with various optical depths, averaged over ocean grid boxes only. Monthly anomalies were computed by subtracting the climatological monthly mean from each respective month of the time series.

multichannel linear regression coefficients are computed as a function of solar and satellite viewing geometry, surface type and PW to predict the CERES observed radiance.

The subfootprint cloud-type derived broadband radiances are then converted to fluxes using the CERES Edition 4 ADM. The sum of derived subfootprint fluxes is then compared with the CERES observed flux. The derived LW flux bias and standard deviation is 1% (2.5 W m^{-2}) and 3% (8 W m^{-2}), respectively. The derived SW bias is within 2.5% (6.25 W m^{-2}) and the standard deviation is mostly within 8% or 20 W m^{-2}, except for clouds with cloud effective temperatures less than 220 K and for thin optical depth clouds (<0.4). It is found that the single cloud-type footprints are not evenly distributed across the globe. The negative regional SW flux biases emanate from partly cloudy footprints and are located in regions with sparse single-scene footprint sampling. The subfootprint fluxes are then normalized or constrained to the observed CERES footprint flux to mitigate any narrowband to broadband flux biases. The instantaneous cloud-type fluxes are then spatially and temporally averaged.

The FBCT and SSF1deg monthly regional fluxes were compared for consistency and to highlight the differences with the CERES SSF1deg product. The FBCT and SSF1deg monthly regional all-sky SW are very similar. The monthly LW fluxes over land are greater in the FBCT than the SSF1deg product, since the FBCT does not include nighttime measurements,

whereas over ocean the LW fluxes are more similar. The FBCT and SSF1deg 18-yr global monthly SW and LW flux anomalies are found to be in good agreement. These results indicate that the FBCT and SSF1deg all-sky flux uncertainties are similar.

Finally, examples of the FBCT data were presented to highlight its utility for scientific applications. The theoretical cloud radiative kernels of Zhou et al. (2013) were compared to a set of kernels computed using the observed FBCT fluxes. Differences between the kernels are attributed to differences in the treatment of clouds, diurnal variations (LW), and how FBCT partitions fluxes among cloud types in the presence of observed clear-sky surface and atmospheric variability. The contributions of different cloud types to Earth's long-term energy budget and their role in transient climate events were also highlighted. For example, positive SST low-cloud radiative feedbacks during the NE Pacific marine heatwave were shown to entail reductions in low-level clouds having medium optical depths. Studies requiring information on cloud-type fluxes will benefit from the FBCT product fluxes (Scott et al. 2020; Myers et al. 2021). The CERES FBCT product is available at the CERES ordering, subsetting, and visualization tool (https://ceres.larc.nasa.gov/data/).

SSF L2 data were obtained from the NASA Langley Research Center EOSDIS Distributed Active Archive Center. We also thank Lazaros Oreopoulos, Mark Zelinka, and an anonymous reviewer for constructive comments on an initial draft manuscript.

REFERENCES

Berry, E., G. G. Mace, and A. Gettelman, 2019: Using A-Train observations to evaluate cloud occurrence and radiative effects in the Community Atmosphere Model during the Southeast Asia summer monsoon. *J. Climate*, **32**, 4145–4165, https://doi.org/10.1175/JCLI-D-18-0693.1.

Boucher, O., and Coauthors, 2013: Clouds and aerosols. *Climate Change 2013: The Physical Science Basis*, T. F. Stocker, Eds., Cambridge University Press, 571–657.

Brodzik, M. J., and J. S. Stewart, 2016: Near-real-time SSM/I-SSMIS EASE-grid daily global ice concentration and snow extent, version 5. NASA National Snow and Ice Data Center Distributed Active Archive Center, accessed 19 February 2022, https://doi.org/10.5067/3KB2JPLFPK3R.

CERES, 2021: CERES_FluxByCldTyp-Day/Month_Ed4A data quality summary. CERES FBCT Rep., 41 pp., https://ceres.nasa.gov/documents/DQ_summaries/CERES_FluxByCldTyp_Ed4A_DQS.pdf.

Cess, R. D., and Coauthors, 2001: Cloud structure anomalies over the tropical Pacific during the 1997/98 El Niño. *Geophys. Res. Lett.*, **28**, 4547–4550, https://doi.org/10.1029/2001GL013750.

Chen, T., W. B. Rossow, and Y.-C. Zhang, 2000: Radiative effects of cloud-type variations. *J. Climate*, **13**, 264–286, https://doi.org/10.1175/1520-0442(2000)013<0264:REOCTV>2.0.CO;2.

Cole, J., H. W. Barker, N. G. Loeb, and K. von Salzen, 2011: Assessing simulated clouds and radiative fluxes using properties of clouds whose tops are exposed to space. *J. Climate*, **24**, 2715–2727, https://doi.org/10.1175/2011JCLI3652.1.

Doelling, D. R., and Coauthors, 2013: Geostationary enhanced temporal interpolation for CERES flux products. *J. Atmos. Oceanic Technol.*, **30**, 1072–1090, https://doi.org/10.1175/JTECH-D-12-00136.1.

Dufresne, J. L., and S. Bony, 2008: An assessment of the primary sources of spread of global warming estimates from coupled atmosphere–ocean models. *J. Climate*, **21**, 5135–5144, https://doi.org/10.1175/2008JCLI2239.1.

Eitzen, Z. A., K. Xu, and T. Wong, 2008: Statistical analyses of satellite cloud object data from CERES. Part V: Relationships between physical properties of marine boundary layer clouds. *J. Climate*, **21**, 6668–6688, https://doi.org/10.1175/2008JCLI2307.1.

——, W. Su, K. Xu, N. Loeb, M. Sun, D. Doelling, F. Rose, and A. Bodas-Salcedo, 2017: Evaluation of a general circulation model by the CERES Flux-by-Cloud-Type simulator. *J. Geophys. Res. Atmos.*, **122**, 10 655–10 668, https://doi.org/10.1002/2017JD027076.

Harrison, E. F., P. Minnis, B. R. Barkstrom, V. Ramanathan, R. D. Cess, and G. G. Gibson, 1990: Seasonal variation of cloud radiative forcing derived from the Earth Radiaiton Budget Experiment. *J. Geophys. Res.*, **95**, 18 687–18 703, https://doi.org/10.1029/JD095iD11p18687.

Hartmann, D. L., M. E. Ockert-Bell, and M. L. Michelsen, 1992: The effect of cloud type on Earth's energy balance: Global analysis. *J. Climate*, **5**, 1281–1304, https://doi.org/10.1175/1520-0442(1992)005<1281:TEOCTO>2.0.CO;2.

Klein, S. A., and C. Jakob, 1999: Validation and sensitivities of frontal clouds simulated by the ECMWF model. *Mon. Wea. Rev.*, **127**, 2514–2531, https://doi.org/10.1175/1520-0493(1999)127<2514:VASOFC>2.0.CO;2.

Kopp, G., G. Lawrence, and G. Rottman, 2005: The Total Irradiance Monitor (TIM): Science results. *Sol. Phys.*, **230**, 129–140, https://doi.org/10.1007/s11207-005-7433-9.

Loeb, N. G., and N. Manalo-Smith, 2005: Top-of-atmosphere direct radiative effect of aerosols over global oceans from merged CERES and MODIS observations. *J. Climate*, **18**, 3506–3526, https://doi.org/10.1175/JCLI3504.1.

——, S. Kato, K. Loukachine, and N. M. Smith, 2005: Angular distribution models for top-of-atmosphere radiative flux estimation from the Clouds and the Earth's Radiant Energy System instrument on the *Terra* satellite. Part I: Methodology. *J. Atmos. Oceanic Technol.*, **22**, 338–351, https://doi.org/10.1175/JTECH1712.1.

——, W. Sun, W. F. Miller, K. Loukachine, and R. Davies, 2006: Fusion of CERES, MISR, and MODIS measurements for top-of-atmosphere radiative flux validation. *J. Geophys. Res.*, **111**, D18209, https://doi.org/10.1029/2006JD007146.

——, B. A. Wielicki, D. R. Doelling, G. L. Smith, D. F. Keyes, and S. Kato, 2009: Toward optimal closure of the Earth's top-of-atmosphere radiation budget. *J. Climate*, **22**, 748–766, https://doi.org/10.1175/2008JCLI2637.1.

——, N. Manalo-Smith, W. Su, M. Shankar, and S. Thomas, 2016: CERES top-of-atmosphere Earth radiation budget climate data record: Accounting for in-orbit changes in instrument calibration. *Remote Sens.*, **8**, 182, https://doi.org/10.3390/rs8030182.

——, and Coauthors, 2018a: Clouds and the Earth's Radiant Energy System (CERES) Energy Balanced and Filled (EBAF) top-of-atmosphere (TOA) Edition-4.0 data product. *J. Climate*, **31**, 895–918, https://doi.org/10.1175/JCLI-D-17-0208.1.

——, T. J. Thorsen, J. R. Norris, H. Wang, and W. Su, 2018b: Changes in Earth's energy budget during and after the "pause" in global warming: An observational perspective. *Climate*, **6**, 62, https://doi.org/10.3390/cli6030062.

——, and Coauthors, 2020a: New generation of climate models track recent unprecedented changes in Earth's radiation budget observed by CERES. *Geophys. Res. Lett.*, **47**, e2019GL086705, https://doi.org/10.1029/2019GL086705.

——, and Coauthors, 2020b: Toward a consistent definition between satellite and model clear-sky radiative fluxes. *J. Climate*, **33**, 61–75, https://doi.org/10.1175/JCLI-D-19-0381.1.

Minnis, P., and Coauthors, 2008: Cloud detection in non-polar regions for CERES using TRMM VIRS and Terra and Aqua MODIS data. *IEEE Trans. Geosci. Remote Sens.*, **46**, 3857–3884, https://doi.org/10.1109/TGRS.2008.2001351.

——, and Coauthors, 2011a: CERES Edition-2 cloud property retrievals using TRMM VIRS and Terra and Aqua MODIS data—Part I: Algorithms. *IEEE Trans. Geosci. Remote Sens.*, **49**, 4374–4400, https://doi.org/10.1109/TGRS.2011.2144601.

——, and Coauthors, 2011b: CERES Edition-2 cloud property retrievals using TRMM VIRS and Terra and Aqua MODIS data—Part II: Examples of average results and comparisons with other data. *IEEE Trans. Geosci. Remote Sens.*, **49**, 4401–4430, https://doi.org/10.1109/TGRS.2011.2144602.

Myers, T. A., C. R. Mechoso, G. V. Cesana, M. J. DeFlorio, and D. E. Waliser, 2018: Cloud feedback key to marine heatwave

off Baja California. *Geophys. Res. Lett.*, **45**, 4345–4352, https://doi.org/10.1029/2018GL078242.

——, R. C. Scott, M. D. Zelinka, S. A. Klein, J. R. Norris, and P. M. Caldwell, 2021: Observational constraints on low cloud feedback reduce uncertainty of climate sensitivity. *Nat. Climate Change*, **11**, 501–507, https://doi.org/10.1038/s41558-021-01039-0.

Ockert-Bell, M. E., and D. L. Hartmann, 1992: The effect of cloud type on Earth's energy balance: Results for selected regions. *J. Climate*, **5**, 1157–1171, https://doi.org/10.1175/1520-0442(1992)005⟨1157:TEOCTO⟩2.0.CO;2.

Ramanathan, V., R. D. Cess, E. F. Harrison, P. Minnis, B. R. Barkstrom, E. Ahmad, and D. Hartmann, 1989: Cloud-radiative forcing and climate: Results from the Earth Radiation Budget Experiment. *Science*, **243**, 57–63, https://doi.org/10.1126/science.243.4887.57.

Rienecker, M., and Coauthors, 2008: The GEOS-5 data assimilation system—Documentation of versions 5.0.1, 5.1.0, and 5.2.0. NASA Tech. Memo. NASA/TM-2008-104606, Vol. 27, 101 pp.

Rossow, W. B., and R. A. Schiffer, 1991: ISCCP cloud data products. *Bull. Amer. Meteor. Soc.*, **72**, 2–20, https://doi.org/10.1175/1520-0477(1991)072<0002:ICDP>2.0.CO;2.

——, and ——, 1999: Advances in understanding clouds from ISCCP. *Bull. Amer. Meteor. Soc.*, **80**, 2261–2287, https://doi.org/10.1175/1520-0477(1999)080<2261:AIUCFI>2.0.CO;2.

Scott, R. C., T. A. Myers, J. R. Norris, M. D. Zelinka, S. A. Klein, M. Sun, and D. R. Doelling, 2020: Observed sensitivity of low-cloud radiative effects to meteorological perturbations over the global oceans. *J. Climate*, **33**, 7717–7734, https://doi.org/10.1175/JCLI-D-19-1028.1.

Soden, B. J., and I. M. Held, 2006: An assessment of climate feedbacks in coupled ocean–atmosphere models. *J. Climate*, **19**, 3354–3360, https://doi.org/10.1175/JCLI3799.1.

——, ——, R. Colman, K. Shell, and J. T. Kiehl, 2008: Quantifying climate feedbacks using radiative kernels. *J. Climate*, **21**, 3504–3520, https://doi.org/10.1175/2007JCLI2110.1.

Su, W., J. Corbett, Z. A. Eitzen, and L. Liang, 2015a: Next-generation angular distribution models for top-of-atmosphere radiative flux calculation from the CERES instruments: Methodology. *Atmos. Meas. Tech.*, **8**, 611–632, https://doi.org/10.5194/amt-8-611-2015.

——, ——, ——, and ——, 2015b: Next-generation angular distribution models for top-of-atmosphere radiative flux calculation from the CERES instruments: Validation. *Atmos. Meas. Tech.*, **8**, 3297–3313, https://doi.org/10.5194/amt-8-3297-2015.

Sun, M., R. D. Cess, and D. R. Doelling, 2012: Interpretation of cloud structure anomalies over the tropical Pacific during the 1997/98 El Niño. *J. Geophys. Res.*, **117**, D16114, https://doi.org/10.1029/2011JD015861.

Sun, W., N. G. Loeb, R. Davies, K. Loukachine, and W. F. Miller, 2006: Comparison of MISR and CERES top-of-atmosphere albedo. *Geophys. Res. Lett.*, **33**, L23810, https://doi.org/10.1029/2006GL027958.

Taylor, P. C., and N. G. Loeb, 2013: Impact of sun-synchronous diurnal sampling on tropical TOA flux interannual variability and trends. *J. Climate*, **26**, 2184–2191, https://doi.org/10.1175/JCLI-D-12-00416.1.

Webb, M. J., C. Senior, S. Bony, and J.-J. Morcrette, 2001: Combining ERBE and ISCCP data to assess clouds in the Hadley Centre, ECMWF and LMD atmospheric climate models. *Climate Dyn.*, **17**, 905–922, https://doi.org/10.1007/s003820100157.

——, F. H. Lambert, and J. M. Gregory, 2013: Origins of differences in climate sensitivity, forcing and feedback in climate models. *Climate Dyn.*, **40**, 677–707, https://doi.org/10.1007/s00382-012-1336-x.

Wyant, M., M. Khairoutdinov, and C. Bretherton, 2006: Climate sensitivity and cloud response of a GCM with a superparameterization. *Geophys. Res. Lett.*, **33**, L06714, https://doi.org/10.1029/2005GL025464.

Young, D. F., P. Minnis, D. R. Doelling, G. G. Gibson, and T. Wong, 1998: Temporal interpolation methods for the Clouds and the Earth's Radiant Energy System (CERES) experiment. *J. Appl. Meteor.*, **37**, 572–590, https://doi.org/10.1175/1520-0450(1998)037<0572:TIMFTC>2.0.CO;2.

Yue, Q., B. H. Kahn, E. J. Fetzer, M. Schreier, S. Wong, X. Chen, and X. Huang, 2016: Observation-based longwave cloud radiative kernels derived from the A-Train. *J. Climate*, **29**, 2023–2040, https://doi.org/10.1175/JCLI-D-15-0257.1.

Zelinka, M. D., S. A. Klein, and D. L. Hartmann, 2012: Computing and partitioning cloud feedbacks using cloud property histograms. Part I: Cloud radiative kernels. *J. Climate*, **25**, 3715–3735, https://doi.org/10.1175/JCLI-D-11-00248.1.

——, and Coauthors, 2020: Causes of higher climate sensitivity in CMIP6 models. *Geophys. Res. Lett.*, **47**, e2019GL085782, https://doi.org/10.1029/2019GL085782.

Zhang, B. C., and Coauthors, 2020: Responses of cloud-radiative forcing to strong El Niño events over the western Pacific warm pool as simulated by CAMS-CSM. *J. Meteor. Res.*, **34**, 499–514, https://doi.org/10.1007/s13351-020-9161-3.

Zhang, M. H., and Coauthors, 2005: Comparing clouds and their seasonal variations in 10 atmospheric general circulation models with satellite measurements. *J. Geophys. Res.*, **110**, D15S02, https://doi.org/10.1029/2004JD005021.

Zhou, C., M. D. Zelinka, A. E. Dessler, and P. Yang, 2013: An analysis of the short-term cloud feedback using MODIS data. *J. Climate*, **26**, 4803–4815, https://doi.org/10.1175/JCLI-D-12-00547.1.